Chemical Engineering Journal 498 (2024) 155144

Contents lists available at ScienceDirect

Chemical Engineering Journal

journal homepage: www.elsevier.com/locate/cej

Transparent coating based on multienzyme-mimicking Janus nanozyme for synergetic biofouling control in seawater

Tao Yu [a], Jiangjiexing Wu [b,*], Yuhe Shen [a], Anastasia Penkova [c], Wei Qi [a], Rongxin Su [a,b,*]

[a] State Key Laboratory of Chemical Engineering, Tianjin Key Laboratory of Membrane Science and Desalination Technology, School of Chemical Engineering and Technology, Tianjin University, Tianjin 300072, PR China
[b] Key Laboratory of Ocean Observation Technology of Ministry of Natural Resources, School of Marine Science and Technology, Tianjin University, Tianjin 300072, PR China
[c] St. Petersburg State University, 7/9 Universitetskaya nab, 199034 Saint Petersburg, Russia

ARTICLE INFO

Keywords:
Marine biofouling
Janus nanozyme
Multiple enzymatic activities
Synergetic antifouling
Transparent coating

ABSTRACT

The problem of marine biofouling persists in marine resource development, particularly for marine observation. While nanomaterials with enzyme-mimicking activity show promise in combating marine biofouling, their unique physicochemical properties that enable nanozymes with multiple enzymatic activities for a synergetic antifouling effect have yet to be explored. Here, it is shown that a transparent zwitterionic coating based on Ag/Ag_2S Janus nanoparticles (Ag/Ag_2S JNPs) with peroxidase-, light-activated oxidase-, and haloperoxidase-mimicking activities contributes to antifouling synergy. The mechanism of the nanozyme action is revealed in a detailed experimental and computational study, in which unique Janus structures guarantee multi-enzyme-mimicking properties and produce •OH, HOBr, and $O_2^{\bullet-}$ to combat biofouling. Through the formation of hydration layers, zwitterionic coatings further enhance this antifouling capacity, as demonstrated by both indoor and outdoor marine field antifouling tests. Consequently, a coating like this shows a clear transmittance and excellent antifouling ability after 90 days in marine immersion, reducing fouling by 74.91 % and 39.71 % compared to a control coating and a commercial coating, respectively. This study not only demonstrates synergetic antifouling actions via multi-enzyme-mimicking activities but also uncovers a new paradigm in nanozyme-based environmentally friendly, sustainable antifouling strategy.

1. Introduction

Ocean development presents a significant challenge to humanity in the form of marine biofouling [1–3]. This biofouling not only disrupts marine activities but also results in substantial human and economic costs [4–8]. As science and technology advance, antifouling technology has expanded beyond traditional domains like shipping and fisheries to encompass optical sensing devices for ocean observation, which necessitate antifouling coatings. In the current antifouling coating system, the two key components are antifouling agents and resins. Existing antifouling agents mainly include copper-based compounds, chemical organic anti-fouling agents, and some natural antifouling agents. Among them, copper-based compound antifouling agents are the most widely used, but research has shown that the long-term accumulation of copper ions can threaten the environment; chemical organic antifouling agents suffer from serious leaching and have a short effective antifouling time; the extraction process of natural anti-fouling agents is complex, leading to higher costs [9]. Therefore, in practical applications, these antifouling agents all have certain drawbacks. Continuing with resin materials, the commonly used ones are side-chain degradable materials. However, this

Abbreviations: Ag/Ag_2S JNPs, Ag/Ag_2S Janus nanoparticles; AIBN, 2,2′-Azobis(2-methylpropionitrile); AJZP, Ag/Ag_2S Janus nanoparticles – zwitterionic polymer; CTAB, hexadecyltrimethylammonium bromide; DMAEMA, dimethylaminoethyl methacrylate; DMPO, 5,5-dimethyl-1-pyrroline N-oxide; EA, ethyl acrylate; EDS, energy dispersive spectrometry; ESR, electron autoselective resonance; FMA, dodecafluoroheptyl methacrylate; FTIR, Fourier Transform Infrared Spectroscopy; HAc, acetic acid; MCD, 2-Chloro-5,5-dimethyl-1,3-cyclohexanedione; MMA, methyl methacrylate; NaAc, sodium acetate; PVP, polyvinyl pyrrolidone; SEM, scanning electron microscope; TAA, thioacetamide; TEM, Transmission electron microscopy; TMB, 3,3′,5,5′-tetramethylbenzidine; UV–vis, Ultraviolet–visible spectroscopy; VASP, Vienna Ab Initio Package; V-BPO, vanadium bromoperoxidase; V-CPO, vanadium chloroperoxidase; XRD, X-ray diffraction; XPS, X-ray photoelectron spectroscopy; ZP, zwitterionic polymer.

* Corresponding authors.
E-mail addresses: wjjx1987@tju.edu.cn (J. Wu), surx@tju.edu.cn (R. Su).

https://doi.org/10.1016/j.cej.2024.155144
Received 6 June 2024; Received in revised form 13 August 2024; Accepted 23 August 2024
Available online 23 August 2024

material tends to dissolve and peel off continuously during use. If this coating is applied in the field of optical sensing, the constantly changing surface of the coating will inevitably affect the detection of optical signals. Additionally, most of these coatings are opaque, adversely affecting light reception by optical sensors. Therefore, there is an urgent need for an environmentally friendly, transparent marine antifouling coating that effectively prevents fouling without compromising the functionality of marine optical instruments [10–14]. Addressing this demand, some researchers have developed transparent coatings. For example, Zhang et al. developed a transparent coating using *SeaNine 211*, applicable to optical lenses. However, the transmittance of the coating decreases as the antifoulant dissolves and releases [15]. Xiao et al. also developed a kind of slippery liquid-infused surface for glass, achieving approximately 88 % transmittance. But, after immersion in seawater for several days, the transmittance gradually declines due to the release of the lubricating liquid [16]. Therefore, in developing transparent marine antifouling coatings, researchers must also consider the potential changes in transmittance over time.

Nature offers many effective and sustainable antifouling strategies, such as biomimetic materials inspired by plants [17,18] and vanadium halide peroxidase from marine diatom [19]. When combined with halide ions (Br^-, Cl^-, *etc.*) and H_2O_2, this enzyme produces hypohalous acid (HOCl, HOBr, *etc.*) and singlet oxygen ($^1O_2$), which inhibits bacterial growth, thus achieving antifouling [20]. However, existing natural enzymes are mainly produced through microbial fermentation for industrialization. The entire process involves multiple steps such as genetic editing, strain improvement, and optimization of culture media. The resulting products also require further separation and purification, making the production process complex and costly [21]. Additionally, due to the complex structure and composition of natural enzymes, they are prone to losing catalytic activity under extreme conditions (such as strong acid, alkali, high temperature, etc.). Based on these two points, the application of natural enzymes in marine antifouling still has limitations.

Recently, nanomaterials with enzymatic functions, termed nanozymes, have garnered considerable attention. These nanozymes couple the unique properties of nanomaterials with the stability, recyclability, and cost-effectiveness of artificial enzymes, opening up a wide range of applications in biomedicine and enviromental protection [21–30]. In particular, several haloperoxidase-mimicking nanozymes have been investigated as a means of combating seawater biofouling [31,32]. Unfortunately, due to the huge difference in activity between nanozymes and nature enzymes, the current developed nanozyme with a single enzyme-mimicking activity is insufficient enough to combat biofouling in complex marine environments. By contrast, the multienzymatic mimicking properties of nanozymes, a result of excellent physicochemical properties of nanomaterials, could be used as-an-antifouling agent in synergetic-fashion. These multienzymatic mimicking properties can help nanozymes better adapt to antifouling requirements in different marine environments, such as: light conditions (light-activated oxidase), dark conditions (haloperoxidase), and freshwater environments like river estuaries (peroxidase). These properties actually provide nanozymes with more potential applications and application scenarios. The exploration of nanozymes that have multienzymatic activity, therefore, is highly desirable for effective and synergistic biofouling control.

In this work, we demonstrate a successful paradigm of Ag/Ag_2S Janus nanoparticles (JNPs), implementing three enzymatic-mimicking activities with zwitterionic polymers to develop a novel transparent antifouling coating, named as the AJZP coating (Scheme 1). This novel Janus structure enabled Ag/Ag_2S to mimic a wide range of enzymes, including peroxidases, light-activated oxidases, and haloperoxidases. To our knowledge, this is the first report of haloperoxidase-mimicking Ag-based nanozymes. Further kinetics, electron spin resonance, and density functional theory simulations were conducted to reveal the multienzyme-mimicking catalytic mechanisms. The use of zwitterionic coatings with formed hydration layers as excellent antibioadhesive surfaces on Ag/Ag_2S reinforced the antifouling ability [33,34]. As tested in lab conditions, the AJZP coating displayed superior antibacterial and antidiatom properties. Another point that needs to be emphasized is that the AJZP coatings possess excellent transmittance, which can meet the needs of some optical devices, and this is exactly what existing commercial coatings are difficult to achieve. We also tested the transmittance of the AJZP coating after 30 days of immersion in seawater. The transmittance of the AJZP coating remained at a high level of 96 %, indicating it is a stable transparent coating. Additionally, real-world seawater tests were conducted to demonstrate antifouling effects of AJZP coating. This work largely addresses the pressing need for transparent antifouling coatings in ocean optical equipment and holds considerable application potential.

2. Experimental section

2.1. Chemicals and materials

All chemicals and reagents were analytical grade. Silver nitrate ($AgNO_3$, 99 %), thioacetamide (TAA, 99 %), polyvinyl pyrrolidone (PVP), (N,N-dimethylaminopropyl) methacrylate, dodecafluoroheptyl methacrylate (FMA), and dimethylaminoethyl methacrylate (DMAEMA) were obtained from Shanghai Aladdin Biochemical Technology Co., Ltd.

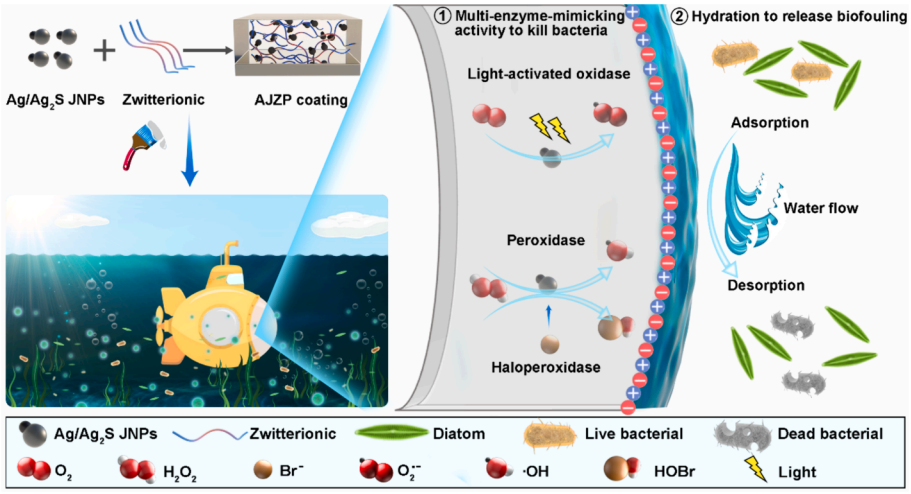

Scheme 1. Schematic illustration of the synergistic antifouling mechanism and marine test of AJZP coating.

(Shanghai, China). Xylene, acetic acid (HAc), nitric acid (HNO_3, 98 %), sodium hydroxide (NaOH, 99 %), isopropyl alcohol, ammonia solution ($NH_3{\cdot}H_2O$, 25 %) and acetone were obtained from Jiangtian Chemical Reagent Co., Ltd (Tianjin, China). Ethyl acrylate (EA), methyl methacrylate (MMA), and 2,2′-Azobis(2-methylpropionitrile) (AIBN) were supplied by Tianjin Kaimate Chemical Reagent Co., Ltd (Tianjin, China). 3,3′,5,5′-tetramethylbenzidine (TMB, 99 %), Sodium acetate (NaAc), 1,3-Propanesultone and hexadecyltrimethylammonium bromide (CTAB, 99 %) were obtained from Tianjin Heowns Chemical Reagent Co., Ltd (Tianjin, China). 2-Chloro-5,5-dimethyl-1,3-cyclohexanedione (MCD), sodium citrate and sodium sulfide (Na_2S) were also supplied by Shanghai Macklin Biochemical Technology Co., Ltd. (Shanghai, China).

2.2. Synthesis of Ag/Ag_2S JNPs, Ag NPs and Ag_2S NPs

Ag/Ag_2S JNPs were synthesized through a one-pot method and all synthesis processes were carried out at 25 °C. The specific synthesis steps were as follows: deionized water (50 mL), hexadecyltrimethylammonium bromide (CTAB) aqueous solution (6 mL, 10 mM), $AgNO_3$ solution (2.705 mL, 10 mM) and $NH_3{\cdot}H_2O$ (5.41 mL, 4 mM) were added into a 100 mL round-bottomed flask in sequence and stirred for 5 min. Then, thioacetamide (TAA) aqueous solution (3 mL, 4 mM) was injected quickly at once, forming brownish complex solution (TAA, with the assistance of CTAB and $NH_3{\cdot}H_2O$, can be used as both a sulfur supplier and a reducing agent). After 24 h of magnetic stirring in the dark, the solution was placed in a dialysis bag (MD44, 500 D), which was then placed in distilled water for 5 d, with distilled water changes every 12 h to remove excess reactants. The washed product was then vacuum-dried for 72 h to finally obtain dark brown Ag/Ag_2S JNPs powder.

Ag NPs were synthesized through a simple hydrothermal method. The specific synthesis steps were as follows: sodium citrate solution (100 mL, 7 mM) and polyvinyl pyrrolidone (24 mg) were added into a 250 mL round-bottomed flask. Then, the pH of the mixed solution was adjust to 8.3 by using NaOH solution. After the pH stabilised, the mixed solution was heated while being stirred. After the mixed solution boiled, $AgNO_3$ solution (1.0 mL, 0.1 M) was added to it and the reaction solution gradually changed from colourless to light yellow. The pH of the reaction solution is then adjusted to 6.1 by using HNO_3 solution, and the solution gradually changes to a cloudy yellow colour, which eventually remains unchanged for a long period of time, a phenomenon that indicates the end of the reaction. Finally, the excess reactants were removed by dialysis, followed by vacuum drying to obtain Ag NPs powder.

Ag_2S NPs were synthesized through a one-pot method and all synthesis processes were carried out at 25 °C. The specific synthesis steps were as follows: Na_2S solution (15 mL, 0.05 M), CTAB (1.09 g) and sodium citrate (96.8 mg) were added into a 100 mL round-bottomed flask in sequence and stirred for 10 min. Then, $AgNO_3$ solution (15 mL, 0.02 M) was slowly added to the reaction solution. At the end of the reaction, the upper solution was taken for centrifugation and vacuum drying to finally obtain Ag_2S NPs powder.

2.3. Measurement of peroxidase-mimicking activity, light-activated oxidase-mimicking activity and haloperoxidase-mimicking activity

The peroxidase-mimicking activities of different catalysts were evaluated by using 3,3′,5,5′-tetramethylbenzidine (TMB) as a substrate in the presence of H_2O_2. The absorbance changes during the reaction process were detected using spectrophotometry. Unless otherwise specified, all reactions were carried out in buffer systems (NaAc–HAc buffer and Tris buffer) at 25 °C. Since the blue oxidized product of TMB exhibits a characteristic absorption peak at 652 nm, the absorbance changes at 652 nm were recorded for all reactions. The measurement of light-activated oxidase-mimicking activity also employed TMB as a substrate, but this reaction did not involve H_2O_2. Additionally, comparative experiments under light and dark conditions were conducted. The remaining test conditions were similar to those of the peroxidase-mimicking activity. The haloperoxidase-mimicking activities of different catalysts were evaluated by using 2-Chloro-5,5-dimethyl-1,3-cyclohexanedione (MCD) as a substrate in the presence of KBr and H_2O_2. The absorbance changes at 290 nm during the reaction were recorded (more details are provided in the ESI). The apparent kinetic parameters for all reactions were calculated based on Hanes-Wolff equation:

$$\frac{[S]}{V} = \frac{1}{V_{max}}[S] + \frac{K_m}{V_{max}} \quad (1)$$

in which ν is the reaction initial velocity, K_m is the Michaelis constant, V_{max} is the maximal reaction velocity, and [S] is the concentration of substance.

2.4. Detection of $^{\bullet}OH$ and $O_2^{\bullet-}$

Electron autoselective resonance (ESR) was used to detect $^{\bullet}OH$ and $O_2^{\bullet-}$ that may be generated by Ag/Ag_2S JNPs. Detection of $^{\bullet}OH$ was performed at 0 min and 10 min after the addition of H_2O_2. Detection of $O_2^{\bullet-}$ was performed at 0 min and 30 min from the start of light exposure. All the tests used 5,5-dimethyl-1-pyrroline N-oxide (DMPO) as the free radical trapping agent.

2.5. DFT calculations

DFT calculations were performed for haloperoxidase-mimicking activity by using the Vienna Ab Initio Package (VASP) software package. More details on the DFT calculations are provided in the ESI.

2.6. Synthesis of AJZP coatings

Xylene (50 g) and acetone (30 g) were added to a 100 mL round-bottomed flask and purged with nitrogen for 20 min in an oil-bath reactor equipped with a thermometer, magnetic stirrer, and reflux condenser. Next, we weighed the monomeric substances for preparing the coating, including: methyl methacrylate (MMA, 15 g), ethyl acrylate (EA, 30 g), 2-methoxyethyl acrylate (5 g), 1,3-Propanesultone (5.8 g), dimethylaminoethyl methacrylate (DMAEMA, 7.5 g), and dodecafluoroheptyl methacrylate (FMA, 22.5 g). Then, the substances other than 1,3-Propanesultone were added to the round-bottom flask and stirred at 60 °C. Thereafter, a mixture of 2,2′-Azobis(2-methylpropionitrile) (AIBN, 0.8 g) and xylene (10 g) was added dropwise in 1.5 h. Following that, the rest of the monomers (1,3-Propanesultone, 5.8 g) and initiator solution (0.3 g benzoyl peroxide dissolved in 10 g of acetone solution) were also added dropwise in 1.5 h. The reaction temperature was then decreased to 40 °C and kept at this temperature for 24 h to obtain the zwitterionic polymer (ZP). The functions of all the above monomeric substances are as follows. Apart from 1,3-Propanesultone, all monomeric substances will serve as the carbon backbone portion of the polymer. Secondly, methyl methacrylate (MMA, 15 g), ethyl acrylate (EA, 30 g) and 2-methoxyethyl acrylate (5 g), primarily function to enhance the adhesion and film-forming properties of the coating. Dodecafluoroheptyl methacrylate is used for reducing the surface energy of the coating by providing a large number of fluorine-containing groups. Dimethylaminoethyl methacrylate and 1,3-Propanesultone are the main components for forming zwitterionic polymers. In turn, the dried Ag/Ag_2S JNPs powder and ZP were blended by ultrasonic vibration with Ag/Ag_2S JNPs powder mass ratios of 0.01 %, 0.05 %, and 0.1 %. Finally, all coatings were prepared by spin coating at a speed of 2500 rpm. The resulting AJZP coatings were placed in a drying oven and dried at 60 °C for 24 h to remove excess solvent.

2.7. Characterization

Transmission electron microscopy (TEM) images were recorded on a JEM-F200 microscope (JEOL, Japan). Powder X-ray diffraction (XRD) data was collected on a Rigaku Smartlab diffractometer. The diffractometer was operated with a scan rate of 2.5°/min (from 20 to 70°). X-ray photoelectron spectroscopy (XPS) was collected using a K-Alpha+ (Thermo, USA). All the measurements were carried out with reference to C 1s binding energy (284.8 eV) as the internal standard. Infrared spectroscopy was carried out on a Nicolet iS50 FTIR spectrometer with coated samples spin-coated on 8 mm diameter glass sheets, using an ATR (Attenuated Total Reflectance) accessory (resolution: 4 cm^{-1}, number of scans: 64, the wavelength range: 4000 to 400 cm^{-1}).The visible spectra of coatings was measured by UV–vis spectrophotometer (Cary 3500, Agilent, USA), and the spectral range was 380–1100 nm. All the coatings were coated on glass, and the visible spectra statistics were used the glass substrate as the baseline. The static water contact angles of coatings were determined by a contact angle goniometer by placing drops of liquid (2 μL) on the surface of coatings at room temperature using sessile method. An average contact angle value was measured from five regions of each sample. The static oil contact angle was measured following a similar protocol. Glycerol and diiodomethane were used as oil. After obtaining the contact angle data, we calculated the surface energy of the coating. We first immersed the coating in seawater, then took the coating out of the seawater at regular intervals within 30 days, and tested the change of the water contact angle of the coating after it was left to dry. The adhesion of each coating on the epoxy resin board was measured by an automatic tester (PosiTest, Model AT-A) according to ASTM D4541-09. Six cylindrical aluminum studs were glued on different regions of each coating and the adhesion strength data was determined by detaching them. The diameter of each stud was 20 mm, and the pull rate was constant at 0.2 MPa/s. We also immersed the AJZP coatings in water for 30 d, periodically sampled from the immersion liquid, and then tested the wash-out of silver ions from the liquid using Thermo iCAP 7400. The specific testing steps are as follows: We spin-coated 0.1 g of the coating on a glass sheet with a diameter of 0.8 cm, then placed it in a 12-well plate, added 3 mL of artificial seawater to each sample well, and incubated it in a constant temperature incubator for static exposure.

2.8. Antibacterial efficiency evaluation

The antibacterial activity of the AJZP coating against Escherichia coli (*E. coli*) was assessed using the standard plate counting assays. Initially, the AJZP coatings were spin-coated onto circular glass sheets with a diameter of 8 mm and dried at 60 °C for 24 h. Subsequently, all AJZP coatings were placed in a suspension of bacterial cells (1×10^6 colony-forming units (CFU)/mL) at 37 °C for 24 h. Then, all the coatings were rinsed with sterile PBS buffer to obtain a PBS solution containing *E. coli*. Finally, 100 μL of the *E. coli*-containing PBS solution was spread onto solid culture medium and incubated at 37 °C for 24 h. White colonies would grow on the surface of the solid culture medium, and the resulting colony count was recorded as U_2. The same procedures were performed on a sterile glass sheet as a blank sample, and the colony count of *E. coli* obtained was recorded as U_1. The antibacterial rate A of the AJZP coatings was calculated by:

$$A = \left(1 - \frac{U_2}{U_1}\right) \times 100\% \quad (2)$$

in which A is the antibacterial rate (%), U_1 is the colony count of blank sample, and U_2 is the colony count of AJZP coatings.

In order to verify the influence of multi-enzyme-mimicking properties on the antibacterial efficiency evaluation, we divided the antibacterial tests of AJZP coatings into four groups by changing the experimental conditions. The first group is the "control" group, with specific testing conditions consistent with the standard plate counting assays mentioned above. The second group is the "H_2O_2" group, where we added a small amount of H_2O_2 to the bacterial cells suspension (resulting in a concentration of 300 μM H_2O_2 in the suspension), with other conditions remaining unchanged. The third group is the "light" group, where we used a 300 W xenon lamp to provide illumination for 8 h, with other conditions remaining unchanged. And the fourth group is the "H_2O_2 + light" group, where we introduced 300 μM H_2O_2 and 8 h of illumination simultaneously in the experiment, with other conditions remaining unchanged. After the completion of the antibacterial tests, we took the antibacterial results of sterile glass slides as U_1, and the results of the other experimental groups as U_2. Then, we calculated the antibacterial rate based on formula (2).

2.9. Antidiatom efficiency evaluation

Nitzschia closterium f.minutissima was used as a model diatom to assess the antifouling performance of all of the films. *Nitzschia closterium* was grown and cultured in F/2 medium without aeration at 21 ± 2 °C with a 12 h/2h light/dark cycle of fluorescent illumination at 2000 lx and gently swayed twice a day. Diatom adhesion was performed using the diatoms in the culture medium. The diatoms reached the logarithmic growth period with a concentration of at least 1.1×10^5 algal cells per milliliter. The test samples (AJZP coating and the pure glass sheet (blank)) were laid on the bottom of the beaker (100 mL), and the beaker was then placed in an illuminated incubator. The samples were incubated for 7 days under the above conditions and then carefully remove from the beaker. The surfaces of all of the samples were washed with deionized water to remove unsettled diatoms. An optical fluorescence microscope was used to observe and record the morphology of the diatoms attached to the substrate. The anti-diatom settled rate was used to express the anti-diatom adhesion performance:

$$r = (1 - \frac{N_2}{N_1}) \times 100\% \quad (3)$$

In which r is the antidiatom settled rate (%), N_1 is the diatom adhesion number of blank sample, and N_2 is the diatom adhesion number of the composite film.

2.10. Marine field tests

Epoxy sheets (50 mm × 50 mm × 3 mm) were coated with AJZP coatings at 25 °C. The sheets were exposed to seawater at a depth of 0.5 m in Bohai Sea (China), where fouling organisms are diversified and biofouling pressure is heavy. The sheets were taken out of the sea periodically and carefully washed with seawater to observe and photograph the deposition of sea organisms and seaweed on the sheets.

3. Results and discussion

3.1. Synthesis and characterizations of the Ag/Ag_2S JNPs

A one-pot method was used to synthesize Ag/Ag_2S JNPs under dark conditions, as shown in Fig. S1 in Supporting information. These JNPs were then characterized using transmission electron microscope (TEM), X-ray diffraction (XRD), and X-ray photoelectron spectroscopy (XPS). Figs. 1a and b, S2 and S3 (Supporting information) demonstrate that asymmetrical, snowman-like Ag/Ag_2S JNPs were synthesized with a mean size of 10.40 ± 1.30 nm. According to Fig. 1c, the XRD pattern of Ag/Ag_2S JNPs matched that of standard monoclinic Ag_2S crystals (JCPDS No. 14-0072) and face-centered cubic Ag crystals (JCPDS No. 04-0783), confirming the successful synthesis of Ag/Ag_2S JNPs. Additionally, Ag_2S (1 1 2) peak at 36.56° and Ag (1 1 1) peak at 38.12° were consistent with high-resolution TEM findings in Fig. S3, in which surrounded Ag_2S and centred Ag had interplanar spacings around 0.25 and 0.23 nm in light- and dark-coloured parts, respectively. It was evident that elements Ag and S are present in Fig. 1d based on an XPS analysis.

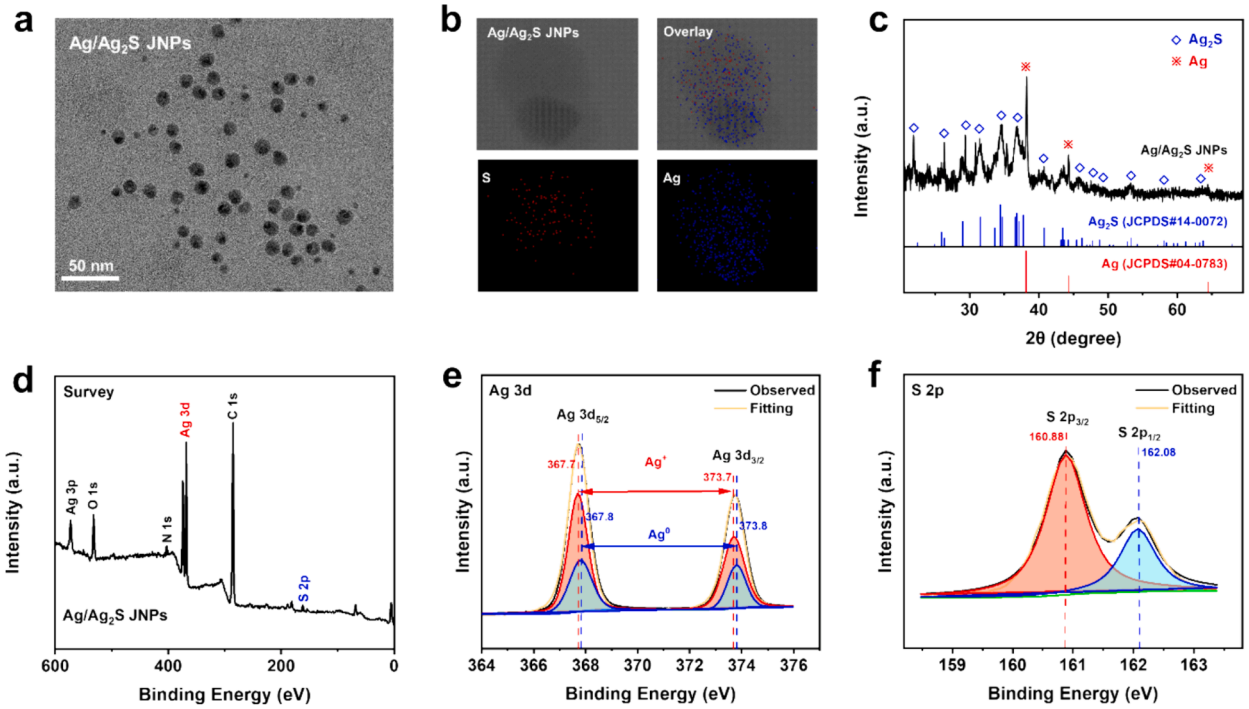

Fig. 1. (a) TEM image of Ag/Ag_2S JNPs. (b) EDS images of Ag/Ag_2S JNPs by TEM. (c) X-ray diffraction pattern of Ag/Ag_2S JNPs. (d–f) Survey and fitted X-ray photoelectron spectra (XPS) measurements of Ag/Ag_2S JNPs (d. Survey scan; e. Ag 3d region; f. S 2p region).

When the XPS results were further fitted to the split peaks (Fig. 1e and f), a combined peak of Ag^0 and Ag^+ appeared with a slight shift, confirming the simultaneous presence of both Ag^0 and Ag^+. Clearly, the nanoparticles we synthesized are a heterogeneous structural composite made up of Ag NPs and Ag_2S NPs, resulting in an asymmetrical morphology. To further substantiate this point, we also utilized TEM to observe and analyze the elemental distribution on the surface of material Ag/Ag_2S JNPs (Fig. S3, Supporting information).

3.2. Measurement of multi-enzyme-mimicking activities

Following successful fabrication of Ag/Ag_2S JNPs, their multi-enzyme-mimicking activities were investigated by monitoring substrate absorbance changes. Fig. 2a shows the peroxidase-mimicking activity of Ag/Ag_2S JNPs using 3,3′,5,5′-tetramethylbenzidine (TMB) as a model substrate. With Ag/Ag_2S JNPs catalysing the oxidation of TMB, blue products with absorption peaks at 652 nm were generated, demonstrating of Ag/Ag_2S JNPs' peroxidase-mimicking properties. Also, control experiments with only Ag NPs, Ag_2S NPs, or no NPs were conducted for comparison. Under the same conditions, Figs. 2b and S4 in Supporting information show that only Ag NPs changed UV–vis spectra at 652 nm in the presence of TMB and H_2O_2, but not Ag_2S NPs or no NPs. Further analysis revealed that the peroxidase-mimicking activity gradually increased when the concentration of Ag/Ag_2S JNPs or Ag NPs was increased (Fig. 2c). According to these results, Ag/Ag_2S JNPs mimic peroxidases, and Ag NPs play a significant role. A similar approach was used to evaluate the oxidase-mimicking activity of Ag/Ag_2S JNPs by monitoring the absorption change at 652 nm of oxidized TMB. As shown in Fig. 2d and e, S5 in Supporting information, Ag/Ag_2S JNPs exhibited nearly negligible activity in the presence of TMB, while a significant enhancement was observed in oxidase-mimicking activity upon visible light (Xenon lamp, 400–700 nm, 300 W) illumination, indicating the visible light could efficiently accelerate the oxidase-mimicking reaction. Gradual enhancement of the visible-light-induced oxidase-mimicking activity was observed as the concentration of Ag/Ag_2S JNPs increased (Fig. 2f). However, for Ag NPs or Ag_2S NPs only, visible light did not enhance absorbance at 652 nm to the same extent as Ag/Ag_2S JNPs (Fig. S5, Supporting information). Consequently, different from peroxidase-mimicking activity, the oxidase-mimicking activity of Ag/Ag_2S JNPs is the result of the joint action of Ag NPs and Ag_2S NPs after forming an asymmetric structure. Interestingly, a similar phenomenon was observed with the haloperoxidase-like activity of Ag/Ag_2S JNPs, where a 2-Chloro-5,5-dimethyl-1,3-cyclohexanedione (MCD) assay was used by monitoring the absorption change at 290 nm of brominated MCD. Fig. 2g–i and S6 in Supporting information demonstrate that Ag/Ag_2S JNPs had an obvious concentration-dependent haloperoxidase-mimicking activity, whereas Ag NPs and Ag_2S NPs had almost no activity.

To identify Ag/Ag_2S JNPs' multi-enzyme-mimicking catalytic mechanism, both experimental and theoretical studies were conducted. First, electron spin resonance (ESR) experiments were performed to monitor the free radical generation ability of Ag/Ag_2S JNPs. In Fig. 3a, a 1:2:2:1 splitting pattern was observed in the presence of H_2O_2, indicating the production of •OH, and a noticeable increase in •OH was also noted with an extended reaction time. In the absence of H_2O_2, no peak was observed, whereas signals of $O_2^{\cdot-}$ was observed with the visible light illumination (Fig. 3b), which explained our earlier conclusion that Ag/Ag_2S JNPs exhibited light-activated oxidase-mimicking activity. Density Functional Theory (DFT) calculations were further carried out to clarify the joint action of Ag NPs and Ag_2S NPs after forming an asymmetric structure. Using experimental results shown in Fig. 1, structural models were constructed for Ag NPs, Ag_2S NPs, and Ag/Ag_2S JNPs (Fig. S7, Supporting information). An example of a haloperoxidase-mimicking catalytic reaction can be seen in Fig. 3c, illustrating the complete catalytic mechanism involving four reaction steps. According to Fig. 3d, Ag/Ag_2S JNPs are more likely to absorb H_2O_2 molecules than Ag NPs or Ag_2S NPs because of their lower adsorption energy (−0.058 eV). Corresponding to this, the adsorption energies of both Ag NPs and Ag_2S NPs are positive (Ag NPs: 0.025 eV; Ag_2S NPs: 0.089 eV). The adsorbed H_2O_2 molecule subsequently produced an adsorbed hydroxyl group (OH*) and a free •OH (Gibbs free energy of this stage: Ag NPs: 0.075 eV; Ag_2S NPs: 0.97 eV; Ag/Ag_2S JNPs: −0.058 eV), followed by oxidizing Br^- to HOBr.

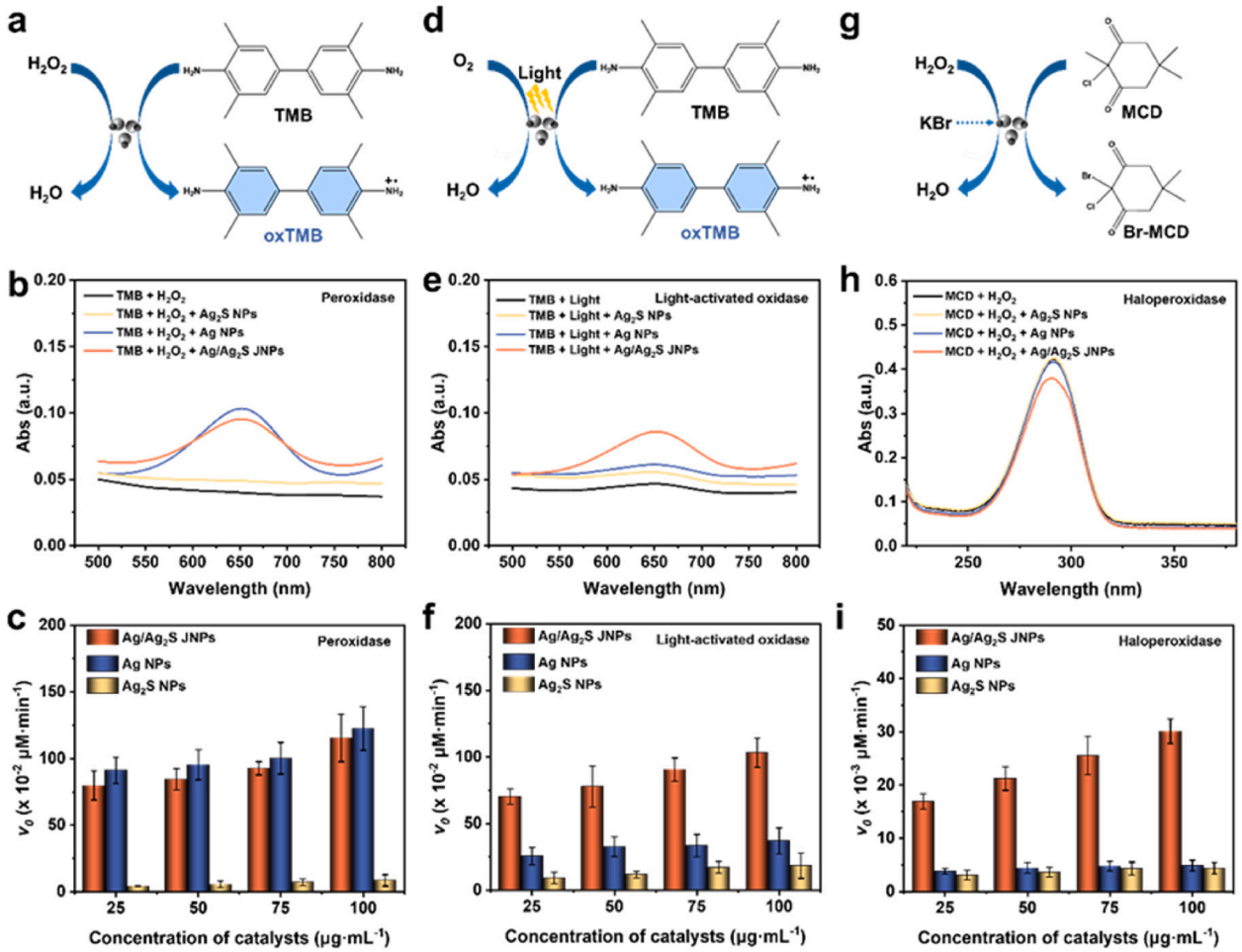

Fig. 2. (a) Schematic illustration of TMB peroxidation catalyzed by Ag/Ag_2S JNPs. (b) Typical absorption spectra of 0.5 mM TMB after catalytic oxidation with 2.5 mM H_2O_2 in pH 3.8 NaAc–HAc buffer at 25 °C, in the presence of 25 μg·mL^{-1} of Ag_2S NPs, Ag NPs, and Ag/Ag_2S JNPs. (c) Initial peroxidase-mimicking velocities of Ag_2S NPs, Ag NPs, and Ag/Ag_2S JNPs at different concentrations. (d) Schematic illustration of TMB oxidation catalyzed by Ag/Ag_2S JNPs under light irradiation. (e) Typical absorption spectra of 0.5 mM TMB after catalytic oxidation in pH 3.8 NaAc–HAc buffer at 25 °C, in the presence of 25μg mL^{-1} of Ag_2S NPs, Ag NPs, and Ag/Ag_2S JNPs. (f) Initial light-activated oxidase-mimicking velocities of Ag_2S NPs, Ag NPs, and Ag/Ag_2S JNPs at different concentrations. (g) Schematic illustration of MCD peroxidation catalyzed by Ag/Ag_2S JNPs. (h) Typical absorption spectra of 100 μM MCD after catalytic oxidation with 2 mM KBr and 20 μM H_2O_2 in pH 8.0 Tris buffer at 25 °C, in the presence of 25μg mL^{-1} of Ag_2S NPs, Ag NPs, and Ag/Ag_2S JNPs. (i) Initial haloperoxidase-mimicking velocities of Ag_2S NPs, Ag NPs, and Ag/Ag_2S JNPs at different concentrations. Error bars indicate standard deviations of three independent measurements.

It appears thermodynamically feasible for HOBr to be produced on Ag/Ag_2S JNPs because of the most negative Gibbs free energy (−1.25 eV). In addition, steady-state kinetics were used to characterize the multi-enzyme-mimicking activities of Ag/Ag_2S JNPs. As shown in Figs. S8–S13 and Table S1 in Supporting information, typical Michaelis–Menten curves were obtained and kinetci parameters (i.e., K_m and V_{max}) were calculated based on Hanes-Wolff linear plots. Considering the multiple enzymatic activities of Ag/Ag_2S JNPs, we selected some typical enzymes to compare with Ag/Ag_2S JNPs (shown in Table S2, Supporting information). In the field of peroxidase-mimicking activities, Fe_3O_4 MNP is a kind of typical nanomaterial. The K_m value of Ag/Ag_2S JNPs for H_2O_2 (6.77 mM) is much lower than that of Fe_3O_4 MNPs (154 mM). Also, the K_m value of Ag/Ag_2S JNPs with TMB as the substrate was 0.38 mM, which was smaller than that of natural HRP (0.43 mM). These results indicate that the Ag/Ag_2S JNPs have a relatively excellent affinity for the substrate, possibly due to their ultrasmall size. When it comes to the light-activated oxidase-mimicking activities, the V_{max} value of Ag/Ag_2S JNPs for TMB is closer to or even better than some common catalysts. What's more, the K_m values of Ag/Ag_2S JNPs for H_2O_2 and Br^- are both lower than those of two biological enzymes—vanadium chloroperoxidase (V-CPO) and vanadium bromoperoxidase (V-BPO). Taken together, we believe that these three catalytic activities of Ag/Ag_2S JNPs are all at a relatively good level, which is sufficient to meet the need of the marine antifouling. We also attempted to test the catalytic performance of the AJZP coating. Even when encapsulated by the polymer resin, the Ag/Ag_2S JNPs still retained certain catalytic capabilities (Fig. S14, Supporting information).

3.3. Synthesis and characterizations of the AJZP coatings

Motivated by the above excellent multi-enzyme-mimicking properties of Ag/Ag_2S JNPs, a transparent antifouling coating based on Ag/Ag_2S JNPs was constructed. Zwitterionic resins have outstanding antibioadhesive properties due to the formed hydration layer, which led us to select the zwitterionic polymer (ZP) coating to strengthen the antifouling capability and ensure long-term efficacy. Following the synthesis pathway depicted in Fig. S15 (Supporting information), four coatings with varying Ag/Ag_2S JNP contents were generated: 0.00 wt% AJZP, 0.01 wt% AJZP, 0.05 wt% AJZP, and 0.10 wt% AJZP. These AJZP coatings were then characterized using Fourier Transform Infrared Spectroscopy (FTIR), scanning electron microscope (SEM), contact angle goniometer, and UV–vis spectrophotometer. Fig. 4a illustrate that FTIR spectrum were similar for four different coatings, and absorption peaks near 3000, 1727, 1455, and 1151 cm^{-1} were attributed to N–H bond

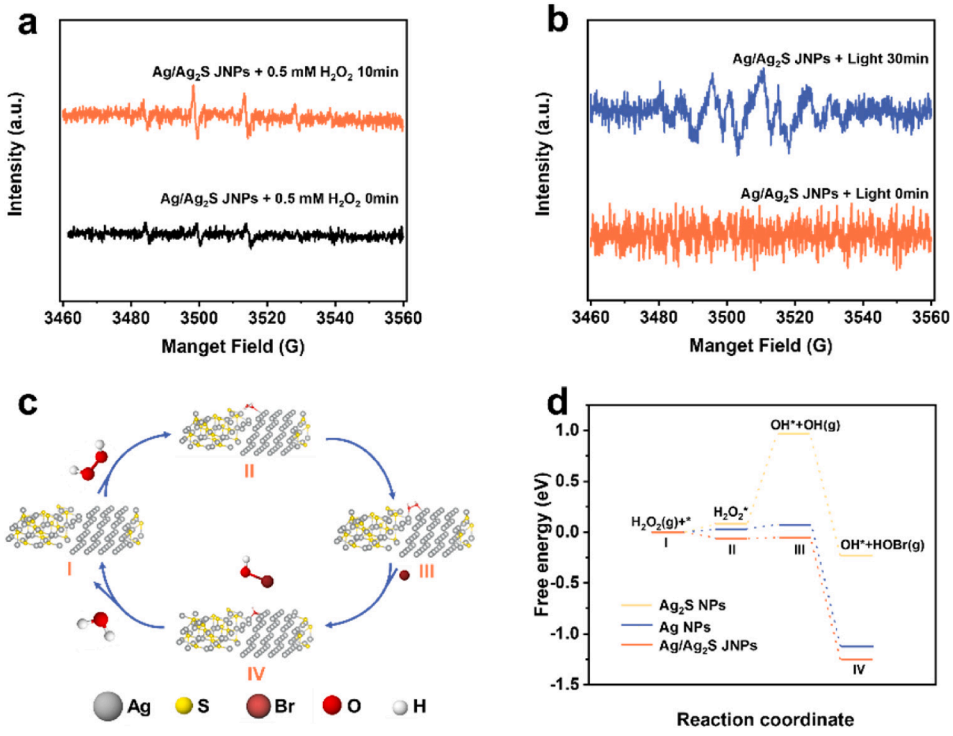

Fig. 3. (a) Detection of •OH by ESR measurement. (b) Detection of $O_2^{\bullet-}$ by ESR measurement. (c) Proposed reaction pathways for bromide oxidation on Ag/Ag_2S JNPs with optimized adsorption configurations. (d) Free energy diagram for Br^- oxidation reaction on AgNPs, Ag_2S NPs and Ag/Ag_2S JNPs.

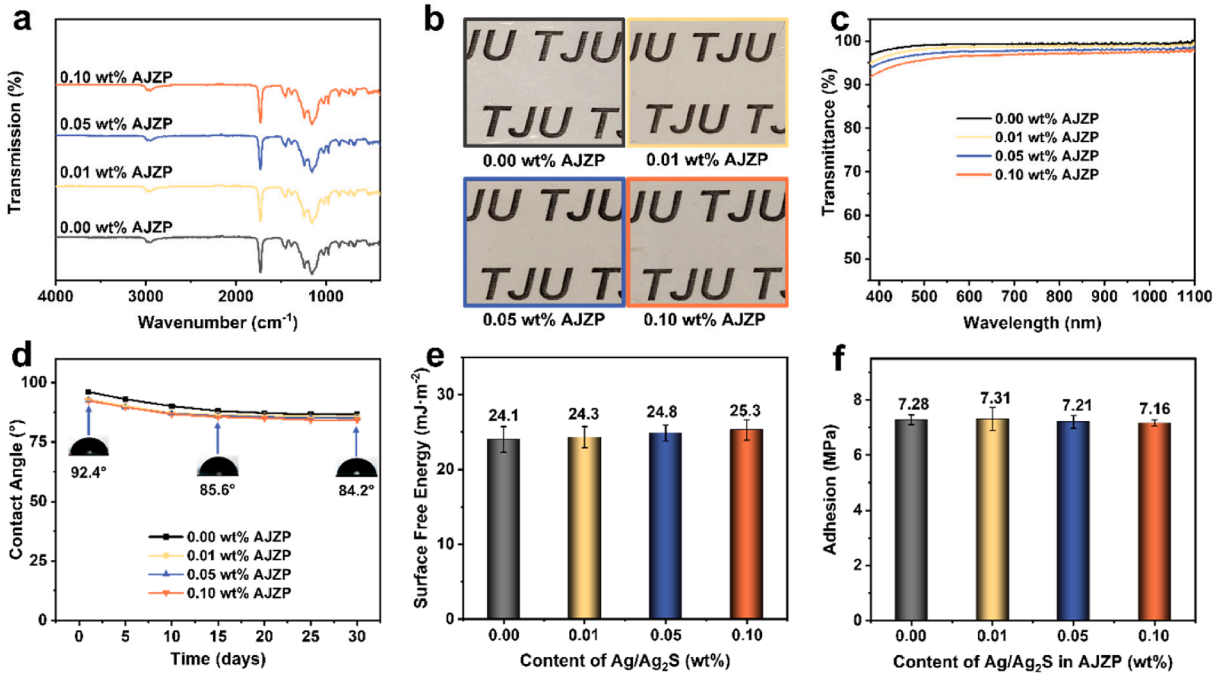

Fig. 4. (a) FTIR spectra of the different AJZP coatings. (b) Transmittance diagram of different AJZP coatings. (c) Transmittance spectra of AJZP coatings. (d) Variation of static water contact angle on the coating surface over 30 days. (e) Surface energy of AJZP coatings. (f) Adhesion of AJZP coatings to epoxy sheet. Error bars indicate standard deviations of three independent measurements.

stretching vibrations, C═O bond stretching vibrations, C–N bond deformation vibrations, and S═O bond vibrations of sulfonates. These results confirmed that coatings formed and that Ag/Ag_2S JNPs had little effect on the integrity of coatings, which is further supported by SEM images (Fig. S16, Supporting information). In addition to the integrity of the coatings, the transmittance was not significantly affected, as shown in Fig. 4b and c. In spite of increased Ag/Ag_2S JNP content, the text behind these coatings could still be clearly seen. A subsequent water contact angle test showed that four coatings exhibited a contact angle around 90° despite a slight decrease in contact angle caused by the addition of Ag/Ag_2S JNPs (Fig. 4d). According to contact angle obtained in Fig. S17, the surface free energy of these coatings was calculated to be

around 25 mJ·m^{-2}, regardless of the Ag/Ag_2S JNPs content (Fig. 4e). Moreover, after measuring the water contact angle, we found that the water contact angle gradually decreased to less than 20° within one minute, which we speculate is because the water drop start to form a hydration layer on the surface of the AJZP coating (Fig. S18 and Movie S1, Supporting Information). In addition, we also observed the cross-section of the coating by SEM, the thickness of the coating is about 5 μm, and the energy dispersive spectrometry (EDS) image proved that the distribution of sliver ions is relatively uniform (Figs. S19 and S20, Supporting information).

In order to ensure long-term practical use, adhesion and stability of these coatings were also assessed. As shown in Fig. 4f, all four coatings showed strong adhesion values of up to 7.31 ± 0.42 MPa, with increasing Ag/Ag_2S JNPs content having no significant effect. This value is already much higher than the adhesion of the similar transparent marine antifouling coating (3.7 MPa) [35], which can meet the daily use of marine antifouling. A 30-day immersion in seawater was conducted to test the long-term stability of these four coatings. After immersion, we tested the coating adhesion and found that it decreased by approximately 3.91 % (0.3 MPa). The coating adhesion still remains around 7 MPa (Fig. S21, Supporting information). According to Fig. 4d, the contact angle of the four coatings decreased rapidly during the first half of the month, but slowly and gradually stabilized during the second half. Compared to the light transmittance of the new AJZP coatings (Fig. S22 and Table S3, Supporting information), Figs. S23 and S24, Table S4 in Supporting information show the light transmittance of these four coatings after immersion. The coating's transmittance decreased slightly after immersion in seawater, but it still maintained a high level of 96 % after immersion. This points to the good transmittance and stability of these coatings. Additionally, we also conducted tests on the light transmittance of AJZP coatings with 0.15 wt% Ag/Ag_2S JNPs, and found that the transmittance decreases with increasing Ag/Ag_2S JNPs content (Fig. S25, Supporting information). What's more, the release of silver ions at ppm levels in Fig. S23 (Supporting information) further confirmed the stability of our fabricated AJZP coatings. Furthermore, following antibacterial and anti-diatom tests, we rinsed and dried the coatings before once again measuring their adhesion and changes in liquid contact angle (Figs. S27 and S28, Supporting information). Numerically, there was no significant difference observed before and after these experiments. Overall, these AJZP coatings were well suited to long-term practical application due to their high adhesion and stability.

3.4. Antibacterial efficiency evaluation

Before exploring long-term practical marine antifouling applications of AJZP coatings, their excellent multi-enzyme-mimicking and anti-bioadhesive properties encouraged us to evaluate their indoor anti-fouling capabilities. Due to bacterial and diatom adherence being critical stages of marine biofouling, laboratory antibacterial and anti-diatom tests were conducted to evaluate indoor antifouling capabilities of AJZP coatings. As shown in Fig. 5, the antibacterial potential of AJZP coatings was determined by plate counting on *Escherichia coli*, a bacterium commonly found in seawater. Considering the synergistic effect of multi-enzyme-mimicking activities of Ag/Ag_2S JNPs, several groups were set and compared (Note: due to the inclusion of halide ions in the experimental conditions, an additional experimental group for adding halide ions is not considered). All our antibacterial rate tests were conducted using sterile glass sheet as the baseline (Fig. S29, Supporting information). A higher antibacterial capacity was found in the H_2O_2 or light groups than in the control group, and this capacity increased with an increase in Ag/Ag_2S JNP content. This dramatic improvement in antibacterial activity is attributed to the generation of •OH and HOBr through peroxidase- and haloperoxidase-mimicking activities, and to the generation of $O_2^{\cdot-}$ through light-activated oxidase-mimicking activities. Combing H_2O_2 with light further enhanced the antibacterial capacity, with the highest antibacterial rate reaching 99.80 % in 0.10 wt% AJZP coating. Notably, after a 30-day immersion in seawater, AJZP coatings still had an antibacterial rate greater than 91.00 % in 0.10 wt% AJZP coating (Fig. S30, Supporting information), indicating their good stability and antibacterial capacity. To further

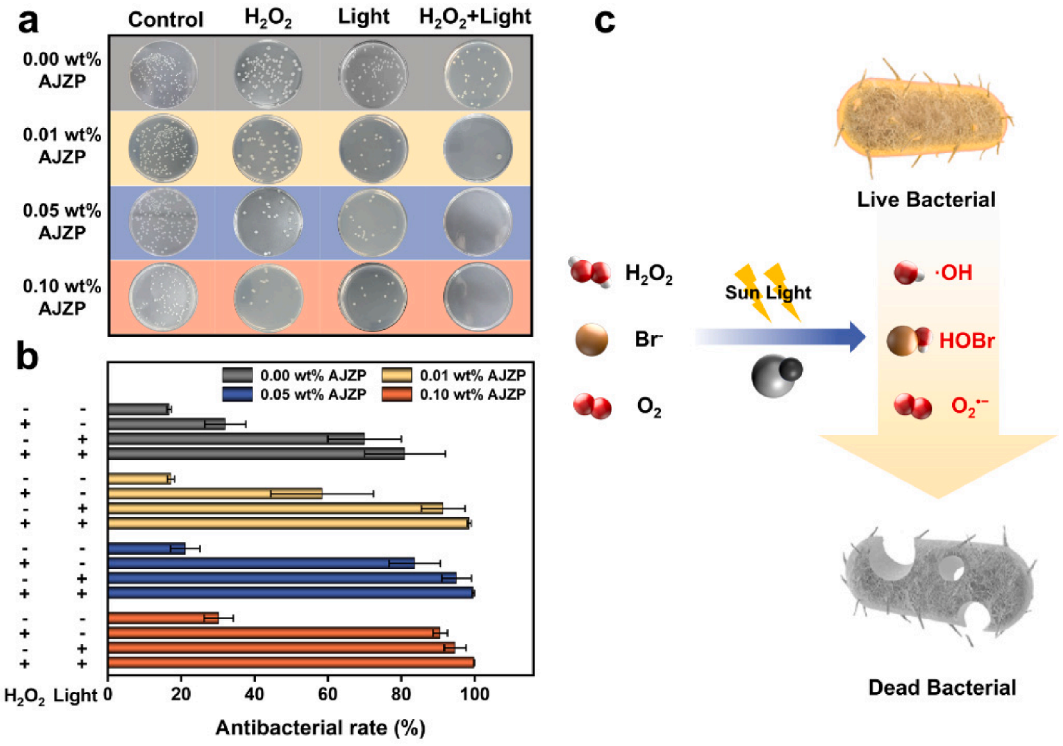

Fig. 5. (a) Antibacterial images of AJZP coatings. (b) Antibacterial rate of different AJZP coatings. (c) Antibacterial mechanism of the AJZP coatings. Error bars indicate standard deviations of three independent measurements.

prove the antibacterial capacity of the AJZP coating, we also used SEM to observe the morphological change of bacteria on AJZP coatings. With the addition of H_2O_2 and light, the density and morphology of the bacteria on the coated surface changed: the density of the bacteria decreased and some of the bacteria were no longer clearly defined, suggesting that this was due to damage and apoptosis of the bacteria (Fig. S31, Supporting information). Moreover, to demonstrate the broad-spectrum antibacterial properties of the AJZP coatings, we conducted antibacterial tests using S. aureus. The testing method was consistent with that used for E. coli, and the results are shown in Fig. S32 (Supporting information). Under the combined action of H_2O_2 and light, the AJZP coating containing 0.10 wt% Ag/Ag_2S JNPs exhibited an antibacterial efficiency as high as 99.7 %. This indicated that the AJZP coatings possess significant broad-spectrum antibacterial capabilities.

3.5. Anti-diatom efficiency evaluation

For assessing the anti-diatom capabilities of AJZP coatings, *Nitzschia Closterium*, a representative marine alga, was selected. According to Fig. 6, after one week immersion in diatom suspension of an exponential growth phase, AJZP coatings were evaluated for their anti-diatom properties by comparing diatom adsorption surfaces. As compared to the bare glass sheet control group, AJZP coatings significantly decreased *Nitzschia Closterium* attachment, which is likely due to the formation of a hydration layer on the zwitterionic polymer surface (Fig. 6a). Furthermore, AJZP coatings' antidiatom capacity increased with increasing JNP content, with the highest antidiatom rate reaching 99.18 % for 0.10 wt% AJZP coating (Fig. 6b). Together, AJZP coatings demonstrated excellent laboratory antibacterial and anti-diatom properties. As a comparison, we supplemented the anti-diatom test of the 0.15 wt% AJZP coating. The specific results are shown in Fig. S33 (Supporting information), indicating that the diatom resistance performance of the 0.15 wt% AJZP coating is comparable to that of the 0.10 wt% AJZP coating.

3.6. Marine field tests

Motivated by the above indoor antifouling results, the long-term practical marine antifouling performance was assessed with marine field tests. To begin with, we selected an environment that was severely fouled, as shown in Fig. S34 (Supporting information). A variety of AJZP coatings, as well as a commercial coating (Jotun SeaForce 60) and a bare epoxy control board were then used in the marine antifouling test. Based on the calculated fouling coverage area, Fig. 7 illustrates the marine antifouling performance of these coatings. A bare epoxy control sheet exposed to the Bohai Sea for 90 days exhibited signs of fouling organisms, with 80.53 % fouling coverage, further validating the heavy fouling environment. Comparatively, in AJZP coatings, fouling coverage area was evidently reduced, and this fouling area decreased with an increase in Ag/Ag_2S JNP content. In particular, the AJZP coating with 0.10 wt% JNP content displayed the best antifouling performance with a proportion of contaminated area close to 5.62 %. It is noteworthy that the antifouling properties of AJZP coatings were even superior to that of commercial Jotun coatings, especially when the JNP content was 0.01 wt%, 0.05 wt%, or 0.10 wt%. To further evaluate the antifouling effect, we observed the biomass on different coating surfaces under a microscope (Fig. S35, Supporting information). Samples were taken from the coating using sterilized cotton swabs and examined under a light microscope. Compared to the blank epoxy resin board, the biomass on the coating surface was drastically reduced. More than 90 % of the surface biomass (most of them are marine diatom and some planktons) was reduced on the coating with 0.1 wt% Ag/Ag_2S JNPs, further demonstrating the coating's impressive marine antifouling effect.

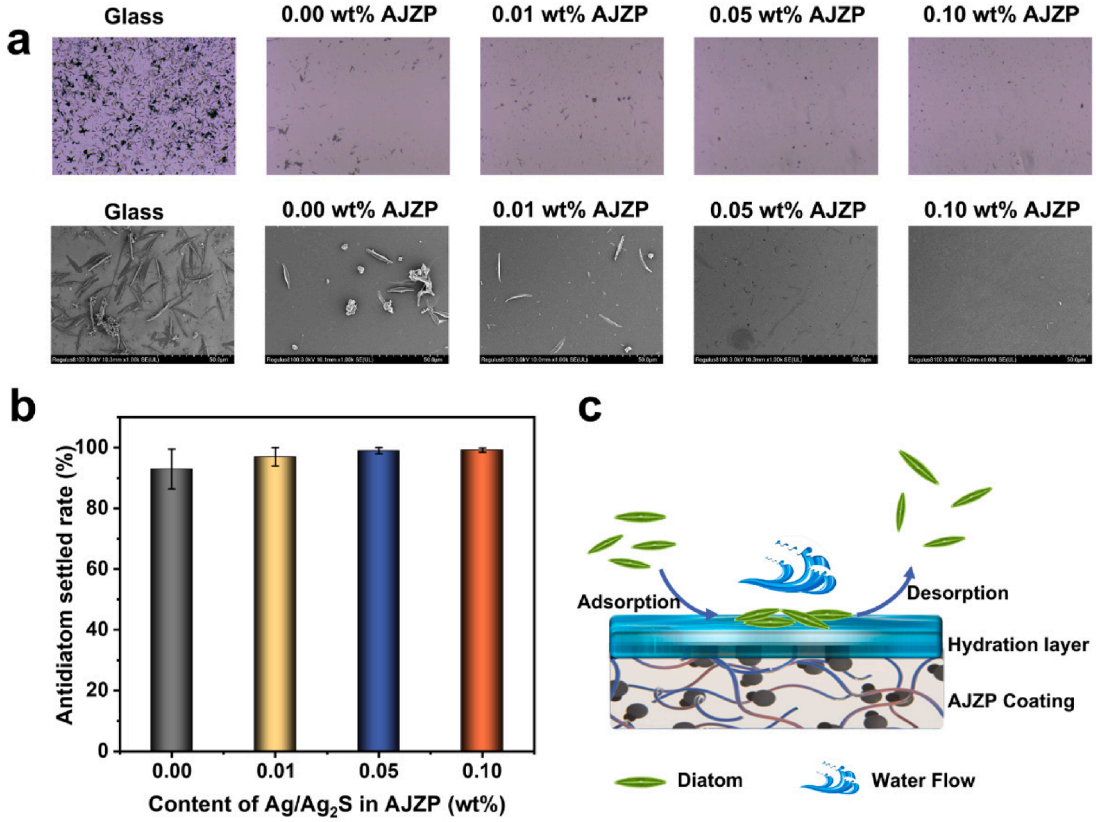

Fig. 6. (a) Optical microscope images and SEM images of the different AJZP coatings. (b) Anti-diatom settled rate of different AJZP coatings. Error bars indicate standard deviations of three independent measurements. (c) Antidiatom mechanism of the AJZP coatings.

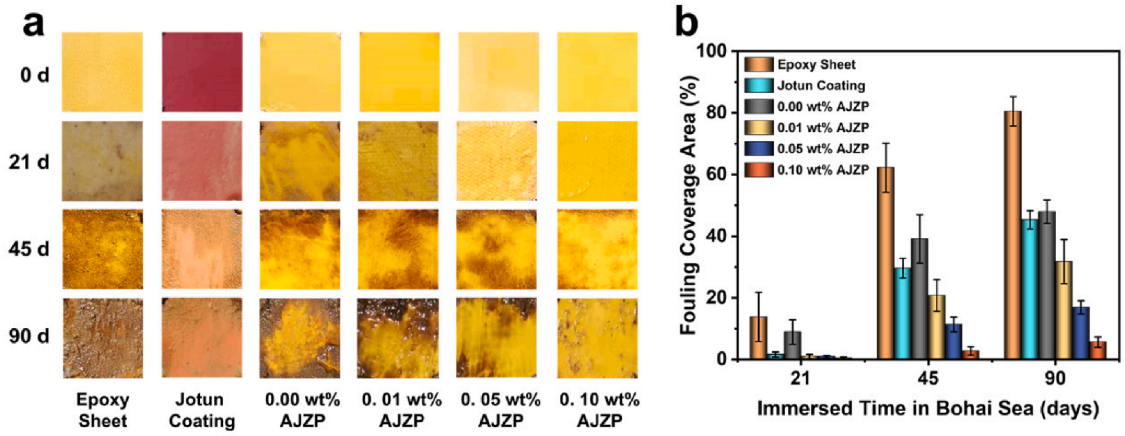

Fig. 7. (a) The surface of different coatings after immersion in seawater for 3 months. (b) Statistics of fouling coverage area of different coatings after immersed in Bohai Sea for 21, 45 and 90 days. Error bars indicate standard deviations of three independent measurements.

4. Conclusion

In summary, we have successfully developed a dense and transparent AJZP coating with multi-enzyme-mimicking activities for synergetic biofouling prevention in seawater, which to our knowledge is the first report on multiple enzyme mimicry in marine antifouling. With Janus structures, peroxidase-, light-activated oxidase-, and haloperoxidase-mimicking Ag/Ag_2S nanozymes were fabricated. Along with its outstanding multi-enzyme-mimicking activity, the AJZP coating also demonstrated excellent transmittance, low surface energy, high adhesion, long-term stability, and eco-friendly, making it the ideal marine antifouling solution. Through the production of $^{\bullet}OH$, HOBr, and $O_2^{\bullet-}$, as well as the formation of hydration layer, AJZP coatings exhibited excellent antibacterial and antidiatom rate, reaching up to 99.80 % and 99.18 %, respectively. In addition to these results, AJZP coatings' effectiveness against marine biofouling was also proven by a marine field test in 90 days, even outperforming Juton commercial coatings. Thus, the study of multiple enzyme mimicry in marine antifouling not only confirms antifouling synergy via multi-enzyme mimicry, but also has the potential to greatly expand the nanozyme-based antifouling technology, allowing it to enrich the current antifouling research.

Author contributions statement

The manuscript was written through contributions of all authors. All authors have given approval to the final version of the manuscript.

CRediT authorship contribution statement

Tao Yu: Writing – original draft, Visualization, Investigation, Data curation. **Jiangjiexing Wu:** Writing – review & editing, Supervision, Conceptualization, Resources, Funding acquisition. **Yuhe Shen:** Investigation. **Anastasia Penkova:** Writing – review & editing. **Wei Qi:** Writing – review & editing. **Rongxin Su:** Writing – review & editing, Supervision, Resources, Funding acquisition, Conceptualization.

Declaration of competing interest

The authors declare that they have no known competing financial interests or personal relationships that could have appeared to influence the work reported in this paper.

Data availability

Data will be made available on request.

Acknowledgements

This work was supported by National Natural Science Foundation of China (52273272, 22378308, and 22104054), Key Program of Tianjin Natural Science Foundation (23JCZDJC00730), and Pandeng program.

Appendix A. Supplementary data

Supplementary data to this article can be found online at https://doi.org/10.1016/j.cej.2024.155144.

References

[1] I. Banerjee, R.C. Pangule, R.S. Kane, Antifouling coatings: recent developments in the design of surfaces that prevent fouling by proteins, bacteria, and marine organisms, Adv. Mater. 23 (2011) 690–718, https://doi.org/10.1002/adma.201001215.
[2] D.M. Yebra, S. Kiil, K. Dam-Johansen, Antifouling technology – past, present and future steps towards efficient and environmentally friendly antifouling coatings, Prog. Org. Coat. 50 (2004) 75–104, https://doi.org/10.1016/j.porgcoat.2003.06.001.
[3] K.A. Dafforn, J.A. Lewis, E.L. Johnston, Antifouling strategies: history and regulation, ecological impacts and mitigation, Mar. Pollut. Bull. 62 (2011) 453–465, https://doi.org/10.1016/j.marpolbul.2011.01.012.
[4] M.P. Schultz, J.A. Bendick, E.R. Holm, W.M. Hertel, Economic impact of biofouling on a naval surface ship, Biofouling 27 (2011) 87–98, https://doi.org/10.1080/08927014.2010.542809.
[5] I. Fitridge, T. Dempster, J. Guenther, R. de Nys, The impact and control of biofouling in marine aquaculture: a review, Biofouling 28 (2012) 649–669, https://doi.org/10.1080/08927014.2012.700478.
[6] E. Almeida, T.C. Diamantino, O. de Sousa, Marine paints: the particular case of antifouling paints, Prog. Org. Coat. 59 (2007) 2–20, https://doi.org/10.1016/j.porgcoat.2007.01.017.
[7] W. Tian, S. Wang, C. Wang, H.R. Xu, Y.F. Zhao, H.C. Jin, L.M. Tian, An epoxy-modified polyurethane composite coating with repetitive self-healing function for anti-cavitation, anticorrosion, and antifouling applications, Chem. Eng. J. 477 (2023), https://doi.org/10.1016/j.cej.2023.146849.
[8] W. Tian, Z.L. Guo, S.L. Wang, H.T. Yu, S. Wang, H.C. Jin, L.M. Tian, Hydrogen and DA bond-based self-healing epoxy-modified polyurea composite coating with anti-cavitation, anticorrosion, antifouling, and strong adhesion properties, J. Mater. Sci. Technol. 187 (2024) 1–14, https://doi.org/10.1016/j.jmst.2023.11.031.
[9] M.Y. Liu, S.N. Li, H. Wang, R.J. Jiang, X. Zhou, Research progress of environmentally friendly marine antifouling coatings, Polym. Chem. 12 (2021) 3702–3720, https://doi.org/10.1039/d1py00512j.
[10] L.D. Chambers, K.R. Stokes, F.C. Walsh, R.J.K. Wood, Modern approaches to marine antifouling coatings, Surf. Coat. Technol. 201 (2006) 3642–3652, https://doi.org/10.1016/j.surfcoat.2006.08.129.
[11] S. Krishnan, C.J. Weinman, C.K. Ober, Advances in polymers for anti-biofouling surfaces, J. Mater. Chem. 18 (2008) 3405–3413, https://doi.org/10.1039/b801491d.
[12] J.A. Callow, M.E. Callow, Trends in the development of environmentally friendly fouling-resistant marine coatings, Nat. Commun. 2 (2011), https://doi.org/10.1038/ncomms1251.
[13] A. Turner, Marine pollution from antifouling paint particles, Mar. Pollut. Bull. 60 (2010) 159–171, https://doi.org/10.1016/j.marpolbul.2009.12.004.

[14] L.M. Gaetke, C.K. Chow, Copper toxicity, oxidative stress, and antioxidant nutrients, Toxicology 189 (2003) 147–163, https://doi.org/10.1016/j.ccr.2015.02.013.
[15] M. Zhang, E. Cabane, J. Claverie, Transparent antifouling coatings via nanoencapsulation of a biocide, J. Appl. Polym. Sci. 105 (2007) 3826–3833, https://doi.org/10.1002/app.26659.
[16] Y.M. Xiao, J. Zhao, R. Qiu, Z.Q. Shi, S.Y. Niu, P. Wang, Slippery liquid-infused surface from three-dimensional interconnecting net structure via breath figure approach and its usage for biofouling inhibition, Prog. Org. Coat. 123 (2018) 47–52, https://doi.org/10.1016/j.porgcoat.2018.06.012.
[17] J. Ma, W.H. Pan, Y.H. Li, J.L. Song, Slippery coating without loss of lubricant, Chem. Eng. J. 444 (2022), https://doi.org/10.1016/j.cej.2022.136606.
[18] J. Ma, J.L. Song, Multifunctional slippery photothermal coating, J. Colloid Interface Sci. 653 (2024) 1548–1556, https://doi.org/10.1016/j.jcis.2023.09.197.
[19] C. Leblanc, H. Vilter, J.B. Fournier, L. Delage, P. Potin, E. Rebuffet, G. Michel, P. L. Solari, M.C. Feiters, M. Czjzek, Vanadium haloperoxidases: from the discovery 30 years ago to X-ray crystallographic and V K-edge absorption spectroscopic studies, Coord. Chem. Rev. 301 (2015) 134–146, https://doi.org/10.1016/j.ccr.2015.02.013.
[20] K. Herget, H. Frerichs, F. Pfitzner, M.N. Tahir, W. Tremel, Functional enzyme mimics for oxidative halogenation reactions that combat biofilm formation, Adv. Mater. 30 (2018), https://doi.org/10.1002/adma.201707073.
[21] H. Wei, E.K. Wang, Nanomaterials with enzyme-like characteristics (nanozymes): next-generation artificial enzymes, Chem. Soc. Rev. 42 (2013) 6060–6093, https://doi.org/10.1039/c3cs35486e.
[22] Y.H. Lin, J.S. Ren, X.G. Qu, Catalytically active nanomaterials: a promising candidate for artificial enzymes, Acc. Chem. Res. 47 (2014) 1097–1105, https://doi.org/10.1021/ar400250z.
[23] L.Z. Gao, X.Y. Yan, Nanozymes: an emerging field bridging nanotechnology and biology, Sci. China-Life Sci. 59 (2016) 400–402, https://doi.org/10.1007/s11427-016-5044-3.
[24] J.J.X. Wu, X.Y. Wang, Q. Wang, Z.P. Lou, S.R. Li, Y.Y. Zhu, L. Qin, H. Wei, Nanomaterials with enzyme-like characteristics (nanozymes): next-generation artificial enzymes (II), Chem. Soc. Rev. 48 (2019) 1004–1076, https://doi.org/10.1039/c8cs00457a.
[25] M.M. Liang, X.Y. Yan, Nanozymes: from new concepts, mechanisms, and standards to applications, Acc. Chem. Res. 52 (2019) 2190–2200, https://doi.org/10.1021/acs.accounts.9b00140.
[26] H. Wang, K.W. Wan, X.H. Shi, Recent advances in nanozyme research, Adv. Mater. 31 (2019), https://doi.org/10.1002/adma.201805368.
[27] B. Unnikrishnan, C.W. Lien, H.W. Chu, C.C. Huang, A review on metal nanozyme-based sensing of heavy metal ions: challenges and future perspectives, J. Hazard. Mater. 401 (2021), https://doi.org/10.1016/j.jhazmat.2020.123397.
[28] Z.R. Wang, Y. Zhao, Y.X. Hou, G.H. Tang, R.F. Zhang, Y.L. Yang, X.Y. Yan, K.L. Fan, A thrombin-activated peptide-templated nanozyme for remedying ischemic stroke via thrombolytic and neuroprotective actions, Adv. Mater. (2023), https://doi.org/10.1002/adma.202210144.
[29] M. Zandieh, J.W. Liu, Nanozymes: definition, activity, and mechanisms, Adv. Mater. (2023), https://doi.org/10.1016/j.cej.2020.124249.
[30] X.M. Shen, Z.Z. Wang, X.J.J. Gao, X.F. Gao, Reaction mechanisms and kinetics of nanozymes: insights from theory and computation, Adv. Mater. (2023), https://doi.org/10.1002/adma.202211151.
[31] F. Natalio, R. André, A.F. Hartog, B. Stoll, K.P. Jochum, R. Wever, W. Tremel, Vanadium pentoxide nanoparticles mimic vanadium haloperoxidases and thwart biofilm formation, Nat. Nanotechnol. 7 (2012) 530–535, https://doi.org/10.1038/nnano.2012.91.
[32] K. Herget, P. Hubach, S. Pusch, P. Deglmann, H. Götz, T.E. Gorelik, I.A. Gural'skiy, F. Pfitzner, T. Link, S. Schenk, M. Panthöfer, V. Ksenofontov, U. Kolb, T. Opatz, R. André, W. Tremel, Haloperoxidase mimicry by CeO_{2-x} nanorods combats biofouling, Adv. Mater. 29 (2017), https://doi.org/10.1002/adma.201603823.
[33] B.W. Li, P. Jain, J.R. Ma, J.K. Smith, Z.F. Yuan, H.C. Hung, Y.W. He, X.J. Lin, K. Wu, J. Pfaendtner, S.Y. Jiang, Trimethylamine N-oxide-derived zwitterionic polymers: a new class of ultralow fouling bioinspired materials, Sci. Adv. 5 (2019), https://doi.org/10.1126/sciadv.aaw9562.
[34] H.C. Guo, Y.C. Fan, Z.H. Sun, Y. Wu, O. Kwon, Phosphine organocatalysis, Chem. Rev. 118 (2018) 10049–10293, https://doi.org/10.1021/acs.chemrev.8b00081.
[35] R.Z. Chen, Y.S. Zhang, Q.Y. Xie, Z.X. Chen, C.F. Ma, G.Z. Zhang, Transparent polymer-ceramic hybrid antifouling coating with superior mechanical properties, Adv. Funct. Mater. 31 (2021), https://doi.org/10.1002/adfm.202011145.